INDENTATION DEFORMATION AND HARDNESS OF CRYSTALS AT LOW LOADS

K. Sangwal

Institute of Physics, Technical University of Lublin, ul. Nadbystrzycka 38,
20-618 Lublin, Poland

Developments in the field of indentation deformation of single crystals at loads ranging from several hundred mN down to a couple of μN are reviewed. Survey of the existing literature shows that the problems encountered in nanoindentation deformation are essentially the same as those investigated during microindentation hardness testing. It is found that refined observation techniques like atomic force and scanning tunnelling microscopy combined with indentation depth sensing techniques provide valuable information about the mechanisms responsible for deformation in the small volumes involved. The experimental observations of recovery of indentation impressions with time may be explained by theoretical models involving generation and multiplication of dislocations and by diffusion processes.

1. Introduction

The mechanical properties of crystalline and non-crystalline substances are closely related with their other physical and electrical properties, and determine the performance of devices prepared from the solids. Consequently, there is a constant interest in assessing the mechanical properties of solids. Experimental techniques involving compression, extension or bending of bulk samples for the determination of the mechanical properties introduce mechanical deformation in the entire bulk and, therefore, are destructive. However, hardness testing, which involves the production of indentations in small areas on the surface by pressing a hard indenter of specified geometry into the solid, is frequently used to assess the mechanical properties. Since the deformed region beneath and around an indentation is confined to a small volume of the solid, the technique is essentially non-destructive. The subject of indentation deformation has also become increasingly important to industries involved with micromachines, microelectronics and magnetic recording.

The scale of indentation hardness testing lies between about 1 mm and 1 nm, and pyramidal indenters are frequently used for indentation. Macroindentation tests using pyramidal indenters are usually carried out at loads P ranging from about 10 to 300 N (1 to 30 kg weight). The diameters of the indentations lie between about 0.1 mm for hard materials and 1 mm for soft materials. Microindentation tests are conventionally carried out at loads between 0.05 and 5 N (5 and 500 g weight). The indentation diameters lie between about 5 and 100 μm. During the last two decades, many works have been devoted to indentation hardness testing using loads between about 1 and 200 mN (0.1 and 20 g weight). For these loads the indentation diameters are usually between 0.1 and 5 μm. Since 1995 indentation deformation experiments have been extended into the range of even still lower loads, from about 1 and 300 μN (0.1 and 30 mg weight). Here the indentation diameters lie between about 30 and 500 nm. In the last two cases of indentations made at loads below about 200 mN where the depths are lower than about 1 μm, one usually refers to nanoindentation deformation.

The hardness H of a solid is defined as its resistance to local deformation. The simplest way to obtain it is to press a hard indenter of known geometry and to divide the applied load P by the area A of the indentation produced, i.e.

$$H = P/A. \tag{1}$$

Obviously, the units of hardness have the dimensions of pressure or stress. Since hardness has dimensions of pressure or stress, attempts have been made to correlate indentation hardness with other stress properties of solids, for example, elastic modulus E, shear modulus G or uniaxial yield stress Y [1-3].

The type of indentation formed depends on the nature of the solid. If the deformation is reversible and determined by classical elasticity theory, the solid is ideally elastic. However, most solids exhibit some ductility. With these solids irreversible deformation occurs beneath the indenter. In practice, under the loads applied for hardness testing no solid is perfect elastic or plastic and all solids exhibit mixed elastic and plastic behaviour. For introduction to the basic concepts of indentation hardness testing, the reader is referred to Refs. [1, 4-6].

The hardness of a material is usually calculated from the measured value of indentation diameter a produced by an applied load P using the relation (1). However, while confronting experimental hardness data with theoretical models, it is usual to use indentation depth d, which is related with diameter a by the indenter geometry. For example, for Vickers pyramidal indenter, $a = 7d$. In the case of macro- and microindentation testings, the indentation diameters and depths are measured using an optical microscope. An optical microscope enables to measure diameters a with an accuracy of ± 1 μm. Therefore, the error in the measurement of diameters of indentations increases with a decrease in their size. At loads in the range of macroindentation, the accuracy in the measurements is better than $\pm 1\%$ in the diagonal and $\pm 2\%$ in the depth. However, in the range of microhardness the accuracy at low loads may be up to $\pm 10\%$ in the diagonal. Consequently, it is expected that the macroindentation hardness is practically independent of load but microhardness either increases or decreases at small loads. In the third case on the other hand, the measurements of a and d are usually made by using scanning (SEM) and transmission electron microscopes (TEM) and atomic force (AFM) and scanning tunnelling microscopes (STM). For the measurements of the depths and diameters of indentations made at very low loads, AFM and STM are conventionally employed. AFM and STM are particularly suited for in situ measurements.

In the field of indentation deformation of single crystals, there are several phenomena which are poorly understood. Among the most widely discussed and controversial topics in the area are the following:
(1) the dependence of microhardness on applied load, a phenomenon known as indentation size effect (ISE) [7-23],
(2) the nature of deformation beneath and around indentations [7,17,23-39], and elastic recovery of hardness strain and changes in the geometry of indentations due to dislocation reactions (i.e. plastic recovery) during unloading [17,27-29,38], and
(3) the mechanism responsible for the appearance of hills piled up around indents [23,25,28, 30,31].

The earlier scientific investigations dealt with microindentation, but recently papers have also been devoted to the study of nanoindentation deformation [9,20-23,25-30,34-36,40-47], comparison of deformation in small volumes with continuum plastic and Hertzian elastic theories [20,22,23,28,30,43-46], and phase transitions [20,21,26,27,47,48] and twinning induced by indentation deformation [17]. Traditional microhardness techniques usually involve measurements of sizes of impressions left after the removal of indentation load. This procedure does not allow to investigate continuous variation of mechanical properties as a function of depth into the test sample or to estimate the amount of elastic recovery occurring in the deformation zone during unloading. Errors of 1-2 μm in the measurements of indentation sizes by optical microscopy limits the indentations of very small sizes in the determination of the properties and hardness of the materials. Nanoindentation (i.e. ultralow load indentation) techniques are capable of providing information as to how the penetration resistance, hardness and elastic properties vary continuously with depth in a sample with resolutions of indenter displacement less than a few nanometers. The separation of load-displacement response into its elastic and plastic components, and the initial stages of plastic deformation is an area of a high research activity.

In this paper developments in the field of indentation deformation of single crystals at loads ranging from several hundred mN down to a couple of µN are reviewed. Observations of nanoindentation deformation at mN and µN loads are reviewed in Secs. 2 and 3, while the kinetics and mechanism of recovery of nanoindentation impressions produced at µN loads are discussed in Sec. 4. Finally, the contents of the paper are summarised in Sec. 5. In the review emphasis has been placed mainly on important problems discussed in the literature rather than compiling a list of references to the works during the last decade. Consequently, omission of papers in the list of references is merely a matter of chance rather than intentional.

2. Nanoindentation deformation at mN loads

2.1. Loading/unloading curves and displacement excursions

Load-displacement curves for a number of materials usually exhibit sudden depth (displacement) discontinuities during loading single crystals to nominal depths of about 50-100 nm [20,21,27,34-36,42,43]. This kind of discontinuities are usually called pop-ins or displacement excursions. Typical load-displacement curves for nanoindentations made on the (100) face of MgO single crystals are shown in Fig. 1a, b and c, while the corresponding atomic force microscopy (AFM) images of the residual indentations are presented in Fig. 2a, b and c, respectively.
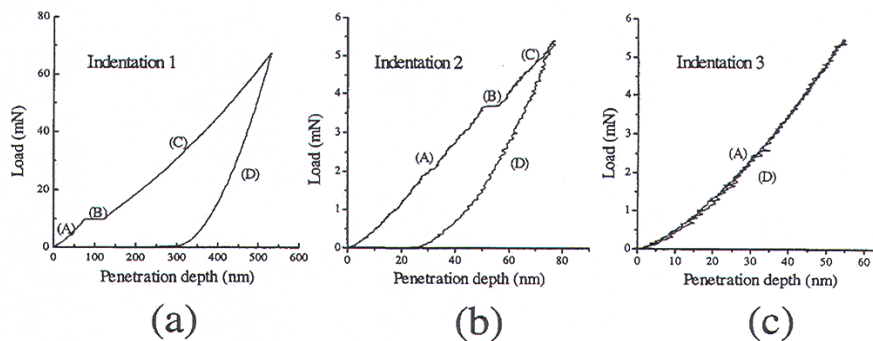

Fig. 1. Typical load-displacement curves for nanoindentations made at loads of (a) 67 mN, (b) 5.5 mN and (c) 5.5 mN on the (100) face of MgO single crystals. Four different stages may be noted in these curves: A: elastic deformation, B: pop-in, C: elasto-plastic deformation, D: elastic unloading. After Ref. [34].

At the highest load (Figs. 1a and 1b), the load-displacement curves exhibit a pop-in and a residual penetration of about 300 nm. At low loads, even at the same value of load, the load-displacement curve shows either a pop-in and a residual penetration (Figs. 1b and 2b) or no pop-in and no residual penetration (Figs. 1c and 2c). In the latter case (Figs. 1c and 2c), an elastic penetration of about 50 nm is observed. These load-displacement curves clearly demonstrate that the pop-in phenomenon is associated with the initial stage of irreversible (plastic) deformation, while the reversible nature of the load-displacement curves in the loading-unloading cycle is due to elastic deformation.
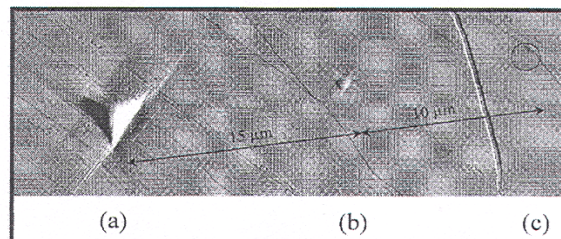

Fig. 2. AFM images of the residual indentations on the (100) face of MgO single crystals, corresponding to the loading-unloading curves of Fig. 1 [34].

Combining surface topography observations by an AFM with load-displacement curves, Tromas et al. [34] demonstrated that the depth of an indentation produced at a particular load and measured by an AFM is equal to the magnitude of the pop-in effect measured from the load-displacement curve. The difference between residual depth measured from a loading-unloading curve and the depth of the pop-in effect corresponds to the depth of rosette arms just close to the indent.

Page et al. [27] reported that, in contrast to other crystals, silicon crystals do not exhibit the pop-in effect during the loading cycle under a Berkovich indenter, but they show sudden reverse depth (displacement) discontinuities for depths exceeding about 100 nm during the unloading cycle. This type of reverse discontinuity during unloading is usually called pop-out effect. Weppelman et al. [20] later confirmed the pop-out effect for Si crystals using a spherical indenter. Recently, Williams et al. [39] examined the loading/unloading behaviour of several compound semiconductors using spherical indenters, and observed the pop-in phenomenon in all crystals. Their study of the loading/unloading behaviour of heavily boron-doped and ion-implanted Si revealed that Si shows both pop-in and pop-out effects.

Page et al. [27] carried out a very comprehensive study of the deformation behaviour of several ceramic crystals using loading-unloading curves and scanning and transmission electron microscopy of deformation structures beneath the indentations. These authors observed that the pop-in during the loading cycle is caused by the nucleation of dislocation loops in the indented surface beneath the indenter, at loads corresponding to the theoretical shear strength of the materials. At higher loads, pronounced dislocation activity and microcracks were observed beneath and around the indentations on the surfaces of crystals which showed the pop-in effect. In contrast to other crystals, silicon showed much less dislocation activity beneath the indentations and residual highly imperfect, amorphous structures within the indentations. The authors attributed the deformation during the loading cycle to a densification transformation occurring at the very high hydrostatic stresses produced under the indenter, and the pop-out effect to the relaxation of densified material during unloading.

Gerberich et al. [42,43] conducted load-displacement experiments on the (100) face of Fe-3wt%Si, the (100) face of Ni and the (111) face of GaAs single crystals using a Hysitron instrument mounted on an AFM and an IBM continuous microindention device. The indentations were made by driving the indenter at fixed rates of about 2 μN/s for the Hysitron instrument (load-controlled) and 1.5-15.0 nm/s for the IBM device (quasi-displacement controlled). The load-displacement curves by the Hysitron instrument reveal the typical pop-in effect while those obtained by the IBM device exhibit a discontinuity with two loads (an upper one at the onset of the discontinuity and a lower one at the end of the discontinuity); Fig. 3. Gerberich et al. [42,43] called them displacement excursions corresponding to the upper and lower yield points. Schematic illustrations of load-displacement curves produced by the load-controlled AFM instrument and the quasi-displacement controlled IBM device are presented in Fig. 4a and b, respectively.
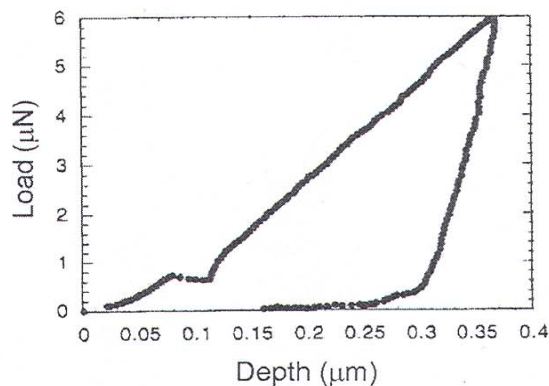

Fig. 3. Load-displacement curve for (111) face of GaAs obtained by the IBM device exhibiting a discontinuity with two loads (an upper one at the onset of the discontinuity and a lower one at the end of the discontinuity). After Ref. [43].
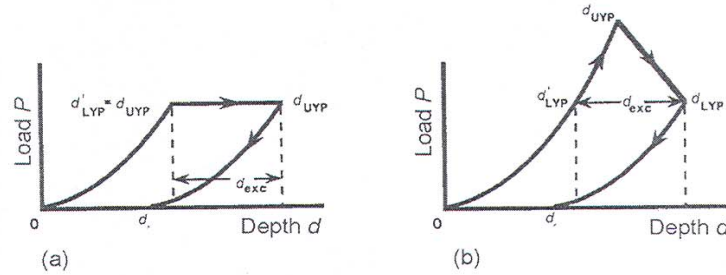
Fig. 4. Schematic illustrations of load-displacement curves produced by (a) the load-controlled AFM instrument and (b) the quasi-displacement controlled IBM device. After Ref. [43].

The mechanism of formation of an indentation on the surface of a crystal at mN loads is considered to involve plastic deformation. Under the indenter tip, first a dislocation loop is nucleated as soon as the theoretical elastic limit is reached. The nucleation of the dislocation loop produces a stress relaxation in the material under the indenter. This is the beginning of the pop-in or displacement excursion. Then the dislocation loop acts as a Frank-Read source, and begins to emit new dislocation loops in succession under this contact surface such that a dislocation pileup is created under the indenter. The dislocation loops expand under the indenter on the slip planes of the primary slip system of the crystal. The relaxation of stress results in a reduction in stress under the indenter. This source operates until an equilibrium between the applied stress σ and the back stress σ_{back} due to the array of prismatic loops is established. The sample is then further loaded, another source is created on a parallel slip band and the previously nucleating dislocations are repelled deeper into the material until another equilibrium is established between σ and σ_{back}. This marks the beginning of the next excursion.

From an analysis of the load-displacement curves for GaAs and Fe-3wt%Si, Gerberich et al. [43] showed the following:
(1) The loading curve up to the upper yield-point load follows the Hertzian theory of elastic contacts.
(2) The lower yield point load P_{LYP} and the upper yield point load P_{UYP} are related with the lower displacement depth d_{LYP}, the upper displacement depth d_{UYP} and the residual depth d_R by an expression similar to that of the Hertzian theory of elastic constants.
(3) The lower yield point displacement d_{LYP} is about twice the excursion width d_{exc} while the residual displacement $d_R \approx d_{exc}$.
(4) The dependence of P_{UYP} and P_{LYP} on d follows an expression similar to the Hertzian theory for elastic contacts ($P \propto d^{3/2}$ for both P_{UYP} and P_{LYP}; see Eq. (8)). This type of relation is expected for the $P_{UYP}(d)$ data but the validity of the same relation for the $P_{LYP}(d)$ data suggests a pseudo-elastic behaviour with elastic-plastic contacts.

The number N of dislocations nucleated at the upper yield point load P_{UYP} and of those supporting the indenter load at the lower yield point load P_{LYP} are related (Fig. 5). This indicates that dislocation-force equilibrium persists in the region of upper and lower yield points.
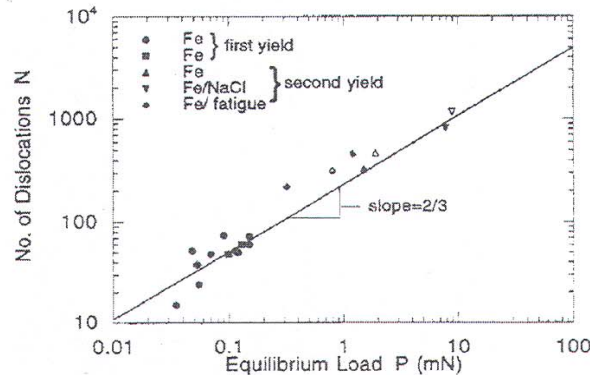

Fig. 5. Relationship between the number N of dislocations nucleated at the upper yield point load P_{UYP} and of those supporting the indenter load at the lower yield point load P_{LYP} [43].

2.2. Dependence of hardness on penetration depth

Hardness is calculated by dividing the applied load by the indentation area. Since indentation area is equal to d^2/B (where d is the indentation depth and B is a constant depending on the type of indenter geometry), it is expected that the values of hardness determined from the load-depth data obtained in the loading cycle are different, depending on whether the displacement corresponds to the moments before and after the displacement excursion. If d_{exc} is the difference between displacements before and after the excursion event and the load-depth data correspond to displacement-controlled curve (i.e. $P_{UYP} > P_{LYP}$; cf. Fig. 4b), then the hardnesses H_{UYP} and P_{LYP} before and after the displacement excursion, may be expressed respectively by

$$H_{UYP} = P_{UYP}/B\, d_{UYP}^2; \qquad\qquad H_{LYP} = P_{LYP}/B(d_{LYP} + d_{exc})^2 \qquad (2)$$

Since $P_{UYP} > P_{LYP}$ and $d_{exc} > 0$, always $H_{UYP} < H_{LYP}$. However, when displacement-controlled loading curves are considered, i.e. when $P_{UYP} = P_{LYP}$ (Fig. 4b), the difference between $H_{UYP} = H_1$ and $H_{LYP} = H_2$ is still smaller but again $H_1 < H_2$. It is interesting to note a similarity between the expression of the relation between hardness H and penetration depth d in the elastic-plastic model of Bull et al. [11] in the form: $P = B'(a + a_0)^2$ (where B' is a constant depending on the indenter geometry, a is the indentation diameter and a_0 is a constant) and the above expression for H_2.

The reported data on P_{LYP} and P_{UYP} for a variety of crystals reveal that the ratio $P_{LYP}/P_{UYP} \approx 2/3$. This is illustrated in Fig. 6. Similarly, the load-displacement plots for GaAs and Fe-3wt%Si single crystals show that the ratio d_{LYP}/d_{UYP} is also approximately equal to 2/3 and $d_{LYP} \approx 2d_{exc}$. This means that $d_{UYP} \approx 3d_{exc}$. Using these approximate relations in the expression for H_{LYP}, one obtains the hardness ratio $H_{LYP}/H_{UYP} \approx 0.375$. For another crystal, if $P_{LYP}/P_{UYP} = 3/4$, $d_{LYP}/d_{UYP} = 3/4$ and $d_{LYP} = 3d_{exc}$, one obtains the hardness ratio $H_{LYP}/H_{UYP} = 0.48$. Similarly, it may be verified that when the ratios are 1/10, $H_{LYP}/H_{UYP} \approx 0.75$; but for a crystal not undergoing plastic deformation, $H_{LYP} = H_{UYP}$.
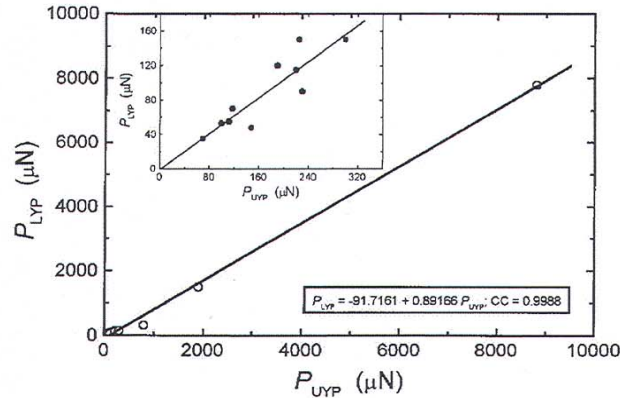

Fig. 6. Plot of P_{LYP} against P_{UYP} for a variety of crystals, showing that the ratio $P_{LYP}/P_{UYP} \approx 2/3$. Inset shows the data close to the origin $P_{LYP} = -1.0883 + 0.5235\, P_{UYP}$; cc = 0.8918. Data from Refs. [42,43].

The plots of hardness H, determined from the load-depth data obtained in the loading cycle, against penetration depth d reveal discontinuities due to the pop-in and pop-out events [21,27,34]. Typical examples of hardness-depth plots from the loading cycle data are illustrated in Figs. 7a and 7b for different samples of GaAs and for MgO crystals.

For undoped GaAs, the pop-in event leads to a large reduction in hardness from a value of 14.6 GPa at the onset of plastic deformation corresponding to a penetration depth d of about 200 nm to about 8 GPa for d exceeding 300 nm (Fig. 7a). The plot shows that hardness H first increases with d up to a certain d corresponding to the onset of plastic deformation, and then, after passing through a maximum, it attains a constant value. Addition of a small amount of In to GaAs suppresses the formation of peak in the $H(d)$ plot for the undoped sample and the penetration depth corresponding to

peak pop-in event is decreased. However, the hardness at high penetrations is not altered by the addition of In. Obviously, addition of In to GaAs leads to more gradual plastic deformation than the overloading behaviour causing the appearance of a peak and abrupt plastic deformation in the case of undoped GaAs crystals.
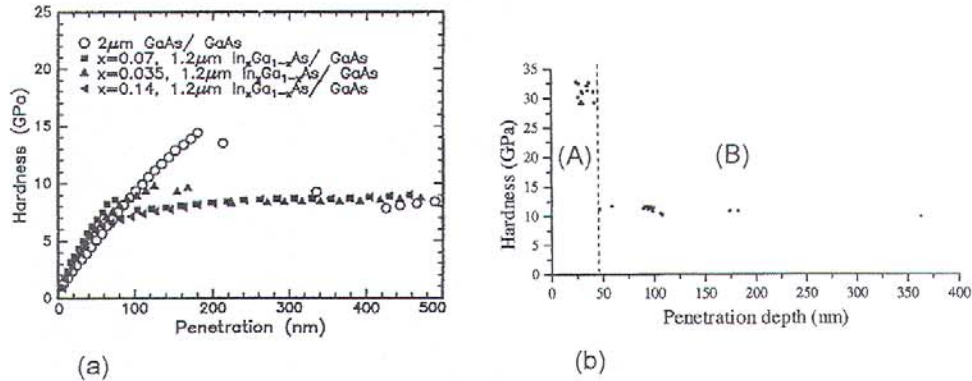

(a)   (b)

Fig. 7. Hardness-depth plots from the loading cycle data for (a) different samples of GaAs with different concentration of In in $In_xGa_{1-x}As$ alloys [21] and (b) MgO crystals [34]. Note that hardness falls down abruptly from 30 GPa at depths below about 50 nm to 12 GPa for depths exceeding 50 nm.

The ability of the appearance of pop-in effect also differs in the case of n- and p-type GaAs crystals. However, in contrast to GaAs crystals, the hardness-depth plot from the loading cycle data for the (001) MgO crystals reveals a high hardness (about 30 GPa) and a low hardness (12 GPa) before and after the pop-in event, respectively. Obviously, the transition between hardness intervals corresponding to the pop-in effect is associated with the nucleation of dislocations beneath the indenter.

An investigation of the influence of elevated temperature implantation and a high dislocation density on the hardness of Si revealed [21] that at room temperature dislocation motion does not play any role in indentation but gross disorder consisting of point-defect clusters lead to some softening. The dependence of hardness on penetration depth for implanted, annealed and dislocation-free Si samples is shown in Fig. 8. As seen from the figure, initially hardness increases with displacement depth up to the depth of the pop-in effect and thereafter it shows a slow increase with penetration depth.
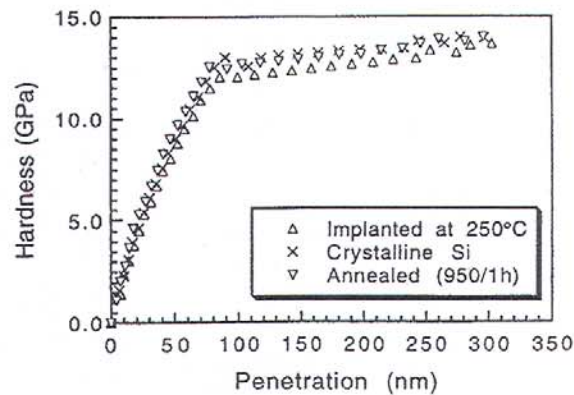

Fig. 8. Dependence of hardness on penetration depth for implanted, annealed and dislocation-free Si samples [21].

Finally, it should be noted that the formation hills of piled-up material during plastic deformation around an indentation is closely related with material glide by the movement of dislocations [24,29,34].

3. Nanoindentation deformation at μN loads

3.1. General features

The first study of nanoindentations was carried out by Lilleodden et al. [30], who made indentations on the (111) face of GaAs single crystals using loads up to several hundred μN loads and explained their observations of the load dependence of indentation size by the Hertzian theory of elastic contacts. Fig. 9 shows the dependence of load P on the depth d of indentations produced by
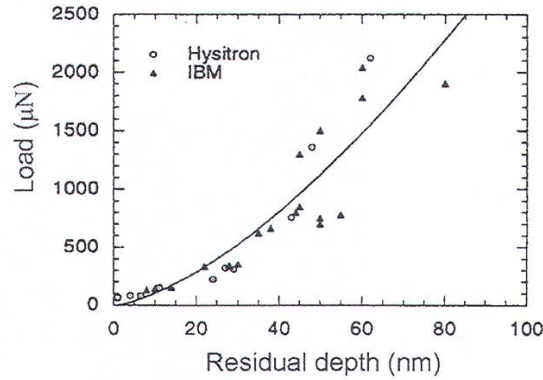

Fig. 9. Dependence of load P on the depth d of indentations produced on the (111) face of GaAs by Hysitron and IBM indenters. The curve represents the best-fit of the data, using the relation between P and d from the Hertzian theory (Eq. (3)). From Ref. [30].

Hysitron and IBM indenters while the curve represents the best-fit of the data, using the relation between P and d from the Hertzian theory [5], i.e.

$$P = (4/3)E^*d^{3/2}R_{tip}^{1/2}, \tag{3}$$

where R_{tip} is the tip radius and the combined (or reduced) tip-crystal elastic modulus is given by

$$\frac{1}{E^*} = \frac{1 - v_{cry}^2}{E_{cry}} + \frac{1 - v_{ind}^2}{E_{ind}}, \tag{4}$$

where E and v with subscripts "cry" and "ind" are the elastic moduli of the crystal and the indenter, respectively.

Nanoindentation experiments on large terrace regions of the (111) surface of Au single crystals revealed [44-46] two distinct regimes of plastic deformation, which are distinguished by the magnitude of discontinuities in load relaxation. In the lower stress region, minor events occur between about 2 and 6 GPa, as illustrated in Fig. 10. In the loading cycle, the dependence of force P on deformation d follows the elastic behaviour predicted by the Hertzian relationship (3) up to about 5 μN where a deviation appears as a change in the load having magnitudes of less than about 5% (change of about 2 nm in deformation). With increasing deformation the force continues to increase according to the Hertzian theory. In the unloading cycle, no discontinuities are observed but some hysteresis is produced. Below about 10 μN, the unloading curve appears approximately parallel with a shift of about 0.5 nm in deformation. It was found that their origin depends on the tip radius, lower tip radius favouring their occurrence. The minor events occur due to nucleation, glide and locking of several dislocations.
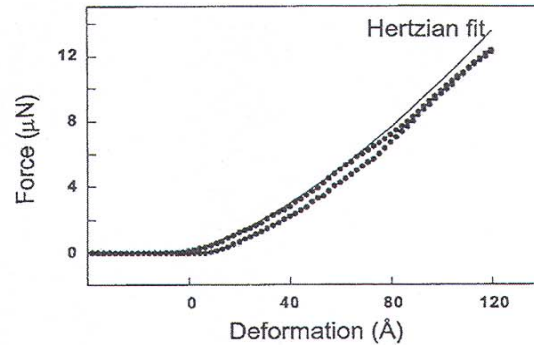
Fig. 10. Loading cycle for the (111) face of Au showing the occurrence of a minor event. The solid line represents the elastic behaviour predicted by the Hertzian relationship (3) up to about 5 μN where a deviation appears as a change in the load having magnitudes of less than about 5% (change of about 2 nm in deformation). After Ref. [45].

It was observed [44-46] that, irrespective of the occurrence of minor events, at higher loads in the loading cycles major events always take place. The load drop in this case often reaches 100%, indicating complete relaxation of the applied load. At still higher loads, yield after the first major event occurs in a series of smaller, discrete events. Fig. 11 shows examples of loading cycles, which were continued well beyond the first major event, on the (111) face of Au. Fig. 11a represents the case of a loading cycle when the terrace width is greater than 500 nm and the indenter is centred between the terrace edges while Fig. 11b shows a loading cycle when the indenter is on a 155-nm-wide terrace, 30 nm from one terrace edge. The figures show that the loading curves represent a combination of elastic and plastic deformation, such that the lattice behaves elastically until some other critical stress is reached when another event occurs. The increment of plastic deformation decreases in magnitude with increasing deformation. In Fig. 11a the unloading cycle was commenced when the applied load reached 35 μN, which gave a total deformation of about 68 nm. The load drop is about 100%. The major events in these figures are associated with the occurrence of dislocation multiplication and generation of mobile dislocations. These dislocations cross-slip, glide and terminate at the surface by surface image force. This results in the formation of a relatively large plastic zone, which enables the elastically stored energy to dissipate in a single event. After the major event, smaller threshold stress necessary to mobilise or further multiply existing dislocations produces smaller events.
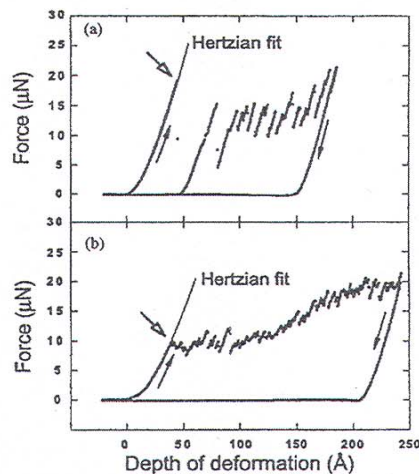

Fig. 11. Examples of loading cycles on the (111) face of Au, showing the effect of steps on plasticity: (a) loading cycle when the terrace width is greater than 500 nm and the indenter is centred between the terrace edges and (b) loading cycle when the indenter is situated on a 155-nm-wide terrace, 30 nm from one terrace edge. Open arrows indicate yield thresholds. From Ref. [22].

The experimental data for the indentation of the (111) face of Au are shown in Fig. 12 as the dependence of R/d on d, while the plot of the ratio a_y/d (where a_y is the contact radius at yield) against d predicted by the continuum theory is presented by the broken line. The yield stress σ_y and contact radius at yield a_y were estimated from the following relations:

$$\sigma_y = P_y/\pi a_y, \tag{5}$$

and

$$a_y = (R_{tip}d_y)^{1/2}, \tag{6}$$

where R_{tip} is the indenter tip radius. The broken line in Fig. 12 shows that the data follow the same functional form but a good fit is obtained when $3a_y/d_{pl}$ is taken as the fitting parameter. This shows that $R_{pl} \approx 3a_y$ throughout the initial stages of plasticity, indicating that the size of the plastic zone is many times the indentation depth.
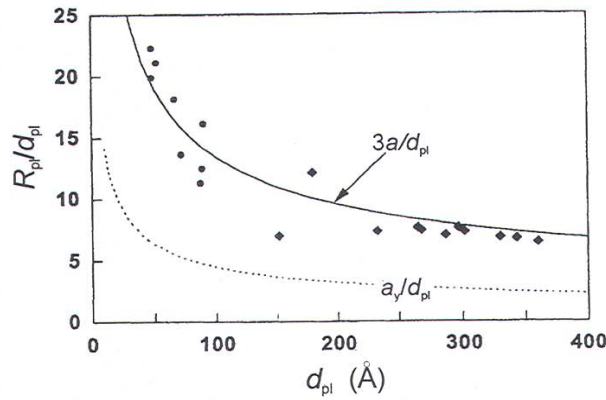

Fig. 12. Experimental data for the indentation of the (111) face of Au shown as dependence of R_{pl}/d_{pl} on d_{pl}, demostrating that the size of plastic zone is many times the size of indention depth. The broken line shows the plot of the ratio a_y/d_{pl} (where a_y is the contact radius at yield) against d_{pl} as predicted by the continuum theory. From Ref. [46].

Corcoran et al [22] observed that nanoindentation load-displacement curves on the (100), (110) and (111) faces of Au in the loading cycle show an interesting yielding behaviour consisting of a series of discrete yielding events separated by elastic deformation (Fig. 13). The first displacement excursion corresponds to the initiation of plastic deformation (yield point). The crystal surface deforms elastically before this plastic deformation as well as in the ascending parts of the loading curve. The number of the displacement excursions and their size changes between indentations but their sum total of the displacements is conserved.
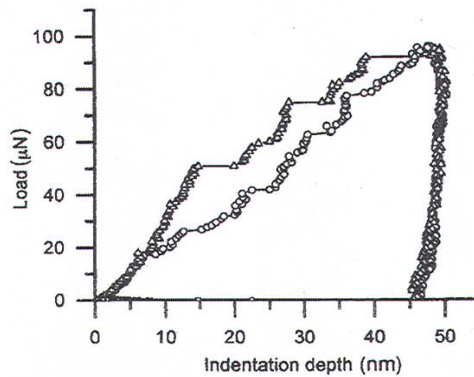

Fig. 13. Load-displacement curves on the (100) face of Au on an atomically flat terrace (triangles) and on a surface with bunched steps (circles). Note a series of discrete yielding events separated by elastic deformation in the loading cycle. The presence of steps facilitates the pop-in effect. From Ref. [22].

The data of $P(l)$ as a function sum of all excursions was analysed by the model of a single displacement excursion. Assuming that the Frank-Read source has pinning points separated by a length equal to the contact radius a_y, the relation between P_{LYP} and the number of dislocations is given by [42,43]

$$P_{LYP} = \frac{3\pi a_y}{2C(\alpha)}\left\{\frac{Gb}{2}\left[1+\frac{N}{\pi(\alpha-1)}\right]\right\},\tag{7}$$

where G is the shear modulus of the crystal, b is the Burgers vector of the dislocation, N is the number of dislocations nucleated at the upper yield point, α is the position of the superdislocation Nb, and $C(\alpha)$ is a geometric factor equal to 0.119 for $\alpha = 4$. The number of dislocations $N \approx d_{LYP}/b$ [43]. Two cases arise from Eq. (7):

(a) When $N/\pi(\alpha-1) \gg 1$ and $a_y^2 \approx 2dR_{tip}$ (see Eq. (6)), one obtains

$$P_{LYP} \approx \frac{3^{1/2}d^{3/2}G}{2}.\tag{8}$$

(b) When the all the plasticity is confined to the displacement excursions of size d, then there are displacement excursions such that for $N = \Sigma d_i/b$ for all excursions to load P_i,

$$P_{LYP} = \frac{3^{1/2}d^{3/2}G}{2}\left(1+\sum(d_i/b)\right).\tag{9}$$

For gold $G = 30$ GPa. Then one obtains

$$P_{LYP}/a_y = 174 \text{ N/m} + 64 \text{ GPa} \sum d_i.\tag{10}$$

Thus, initiation of a Frank-Read source and its subsequent multiplication, as represented by case (b), may be used to explain the experimental data of discrete yielding events.

Fig. 14 show a plot of P/a_y against Σd_i for indentations on the (100), (110) and (111) faces of gold. For the plot, the constant is 242 N/m while the slope is 7.5 GPa. This suggests that stress necessary to activate the Frank-Read source is in good agreement with the predicted value. However, the value of the slope is much lower than the predicted value. This discrepancy is associated with the interaction of dislocations on parallel slip planes.
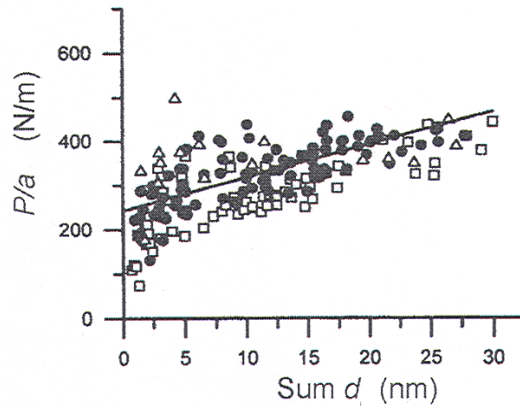

Fig. 14. Plot of P/a_y against Σd_i for indentations on the ($\square$) (100), ($\bullet$) (110) and ($\triangle$) (111) faces of gold, according to Eq. (10). After Ref. [22].

The value of the yield point decreases with the presence of steps on the surface being indented (Figs. 11 and 13. The reason of a lower yield stress is that steps act as nucleation sites for dislocations.

When the yielding behaviour of a crystal at the onset of plastic deformation (at the time of onset of the pop-in effect) occurs in a series of discrete yielding steps, substantially different values for hardness are obtained, depending on whether an indenter is unloading before or after the displacement excursion. This behaviour is shown in Fig. 15. The figure shows that, corresponding to a particular displacement d, the hardness H_2 after the displacement excursion is lower than the hardness H_1 before the excursion. This behaviour follows from Eq. (2). A gradual decrease in H with increasing d (i.e. normal indentation size effect; normal ISE) is evident from the plots. Moreover, H_2 approaches H_1 when penetration depth is relatively large and H is practically independent of penetration depth (i.e. load).
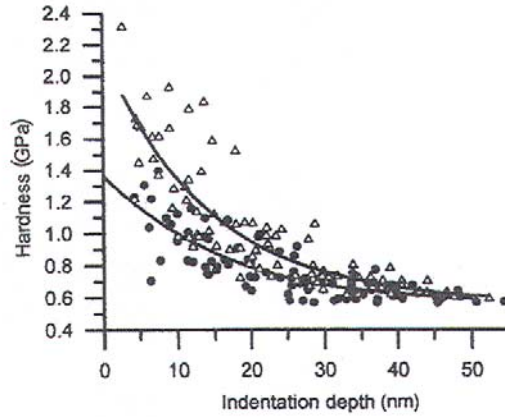

Fig. 15. Hardness values obtained from indentation curves on the (100) face of Au. The hardness was calculated from geometric area of indentations at depths before (Δ) and after ($\bullet$) i excursions. After Ref. [22].

Recently, Sangwal and his coworkers [23] carried out a detailed investigation of the indentation deformation of (100) face of MgO at μN loads and, using theories of elastic and plastic deformation, analysed the experimental data of the penetration depth d of the first indents scanned by an atomic force microscope immediately after indentation, their diameter a, the radius R of deformation zone, and the height h of hills pile-up around them (Fig. 16a).

The relationships between the measured indenter penetration depth d, the indentation diameter a, the deformation zone radius R, and the average height h of indentation hills are shown in Fig. 16b. It is obvious from the figure that these relations may be expressed by the equation

$$y = y_0 + kd = k(y_0 + y) = kd^*, \tag{11}$$

where k is the ratio of y to d for $y > y_0$, d_0 is the threshold value of d beyond which the linear relationships are valid, and $d^* = (d_0 + d)$ is the corrected indentation depth. Moreover, hill height h also linearly increases with a for $a > a_0$.

It may be seen from Fig. 16b that a threshold force is necessary to make an indent. For the indenting tips used on MgO crystals this threshold pressure (calculated from applied load P and nominal tip radius $R_{tip} = 10$ nm) was about 3 GPa. Moreover, as seen from Fig. 16, the values of d_0 obtained from $R(d)$ and $a(d)$ plots are 26.6 and 26.3 nm, while that obtained from $h(d)$ plot is practically zero. Using the value of a_0 and the corresponding d_0, one may also obtain the value of the semiapical angle $\beta = \tan^{-1}(a_0/2d_0)$.
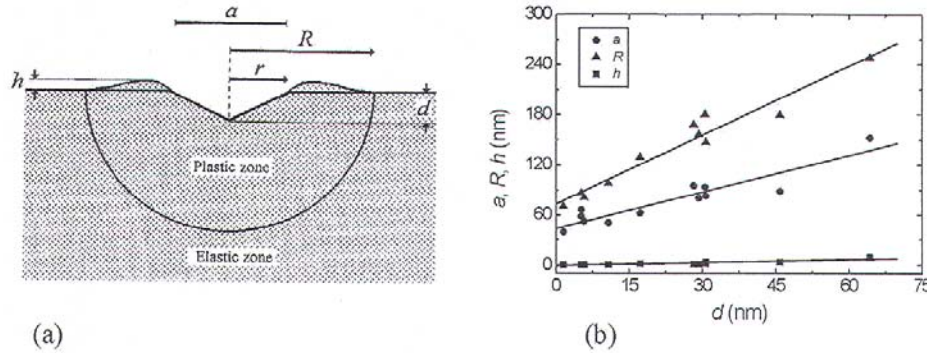
Fig. 16. (a) Schematic illustration of experimental quantities involved in an indentation. (b) Dependence of indentation diameter a, deformation zone radius R, and the average height h of indentation hills on indenter penetration depth d on the (100) face of MgO. Note that all the parameters are linearly related with d and that a threshold force is necessary to make an indent. After Ref. [23].

For indentations on the (100) face of MgO, the ratio R_0/r_0 (also the ratio R/r) of the radius of deformation zones to that of indents is 3.3 (i.e. $R/a = 1.67$). This value is comparable with the ratio of size of dislocated region and diagonal of Vickers indenter in the range of microindentations into the (100) face of Fe-3%Si [28] and with the ratio of the plastic zone to the indentation contact radius for the (111) face of Au, Fig. 12 [46]. However, in contrast to indentation deformation involving dislocations in Fe-3%Si, no slip lines indicating the generation of dislocations on the surface surrounding indents were observed.

The above results show that, although a, R and h linearly increase with d, there are two different processes involved during indentation. The first is associated with the development of indentation size and deformation zone, while the second is associated with the formation of hills, which occurs as soon as the threshold d_0 is attained. The $R(d)$ and $a(d)$ relations reveal that the deformation zone sets in (i.e. $R \geq 0$) when $a = 0$.

It is interesting to note that, although the elastic modulus E of Si is lower than that of MgO, Si tips produce indentation imprints on the (100) face of MgO. From a consideration of the values of the elastic moduli ($E(\text{Si}) = 166$ GPa and $E(\text{MgO}) = 286$ GPa [49]) it is expected that Si tips undergo plastic deformation which will lead to an increase in the tip radius during successive indentations. In the experiments no such changes in the radius of a tip were recognised from the load threshold checked before and after indentation. This observation may be explained from a consideration of the reduced tip-crystal elastic modulus E^*, given by Eq. (3). Using the values of $E(\text{Si})$ and $E(\text{MgO})$ given above and taking $\nu_{\text{cry}} = \nu_{\text{ind}} = 0.3$, one obtains $E^* = 115$ GPa. This reduced E^* is lower than the values of both $E(\text{Si})$ and $E(\text{MgO})$. This suggests that the ability of indentation of a tip of elastic modulus E lower than that of the crystal is determined by the reduced tip-crystal elastic modulus E^*.

The experimental data of the dependence of a, d and R on load P may be analysed using different theoretical models. For rigid plastic materials, Tabor [1,4] gives a relation between indentation load P and indentation diameter a for a conical or pyramidal indenter in the form

$$P = H_M \pi a^2 / 4 = 0.785\, H_M\, a^2, \tag{12}$$

where H_M is the Mayer hardness of the material. In Eq. (12) it is assumed that $H \approx 3Y$. According to Johnson's cavity model [5,28,30], the relation between applied load P and deformation zone radius R is given by:

$$P = 2\pi Y R^2 / 3 = 2.1 Y R^2, \tag{13}$$

where Y is the yield stress of the material under investigation. Moreover, the dependence of depth d^* on applied load P was analysed according to the Hertzian theory for elastic contacts (see Eq. (3)). Fig. 17a shows the plots of P against a^2 and R^2 while Fig. 17b shows the plot of the dependence of P on $d^{3/2}$. It may be seen from the plots of these figures that, as expected from Eqs. (12), (13) and (3), P is linearly related with a^2 and R^2 and with $d^{3/2}$.

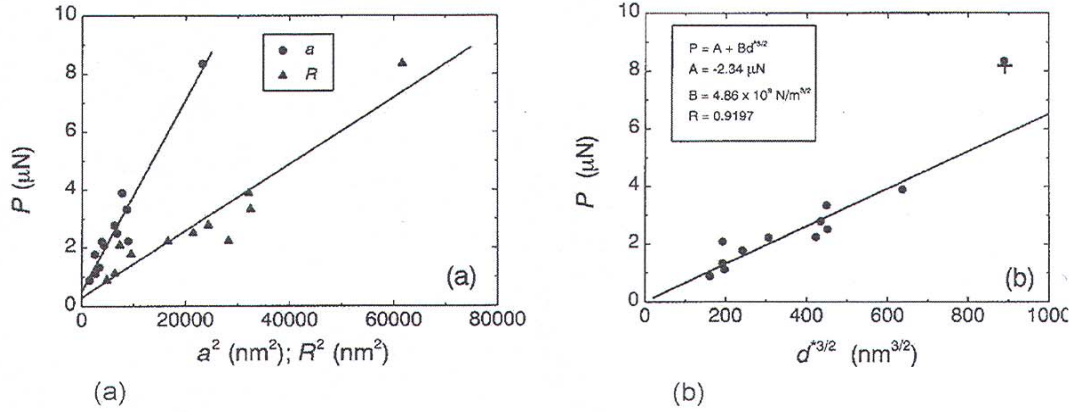(a)   (b)

Fig. 17. Plots of the dependence of applied load P on (a) a^2 and R^2, and (b) $d^{*3/2}$ for the experimental data obtained on the (100) face of MgO (see Fig. 16). After Ref. [23].

It was observed [23] that the Meyer hardness H_M obtained from Tabor's relation is lower by a factor of 10 to 20 than the literature value [11,24,50], which lies between 4 and 8 GPa. The value of the yield point $Y = 55$ MPa obtained from Johnson's cavity model is close to the value of 80 MPa reported in the literature [51]. The slope of the plot of the Hertzian relation is 4.86 N/m$^{3/2}$ which gives $E^* = 36,450$ GPa for the tip radius $R_{tip} = 10$ nm. This value is higher than the actual value of $E^* = 115$ GPa by a factor of 320. These results show that Tabor's model for perfect rigid plastic solids explains the nanoindentation data on MgO crystals when $H = 30Y$ to $60Y$, and that Johnson's cavity model reasonably well describes the experimental $P(R)$ data. However, the Hertzian theory gives the worst agreement with the experimental data.

The hardness stresses H involved during the nanoindentation of the (100) face of MgO lie between 300 and 900 MPa. These stresses are higher by a factor of 4 to 12 than the reported yield point Y [51] and are lower by a factor of 10 to 25 than the reported microhardness of MgO crystals [11,24,50]. This means that nanoindentation stresses here lie between stresses involved in inducing plastic deformation and producing microindentations accompanied by plastic deformation (slip lines). However, since slip traces due to the generation of dislocations were not observed on the surfaces, it was concluded [23] that the generation of dislocations is not essential for the observation of ISE during nanoindentation. The large discrepancy between nano- and microhardness is due to the assumption that the ratio of hardness H to yield stress Y is 3 (for example, in Tabor's model for rigid plastic solids; Eq. (12)). For most crystals $H/Y \approx 35$ [1,52].

Apart from the elastic stage in which Hooke's law holds (i.e. ratio of stress to strain is equal to Young's modulus E), the stress-strain behaviour of plastic crystals shows at least four stages with differing work-hardening coefficients θ [53]. The hardening coefficients in stages I and II are constant and are associated with easy glide and multiple slip, respectively. However, in stages III and IV the hardening coefficients decrease with increasing strain. These latter stages of decreasing work hardening involve cross-slip and redistribution of defects (dislocations and point defects) produced during deformation into configurations with lower energy (polygonisation and annihilation of dislocations).

There is a similarity between different stages of stress-strain curves and the dependence of hardness stress on hardness strain. Therefore, for the purpose of comparison, it is sufficient to consider the strain-dependent hardening coefficients of stages II and III.

Following Gil Sevillano [53], the dependence of coefficient $\theta = \sigma_H/(a/2R_{tip})$ on hardness stress σ_H (see Sec. 4.3) may be given by

$$\theta = \theta_0\left(1 - \sigma_H / \sigma_{Hs}\right), \tag{14}$$

where θ_0 corresponds to the hardening coefficient at zero stress, and σ_{Hs} is a saturation stress.

Fig. 18 shows the plot of the dependence of θ on σ_H. From the plot one obtains $\theta_0 = -147.7$ MPa and $\sigma_{Hs} = 260.4$ MPa. In contrast to positive values of θ_0 observed in stress-strain curves where strain hardening takes place, here θ_0 is negative. The negative value of θ_0 means that softening occurs during normal ISE. The value of σ_{Hs} is comparable with the value of load-independent hardness σ_H at $a \to \infty$, obtained from the general equation of models which do not involve the generation or presence of dislocations (see Eq. (13)). One also finds that $\sigma_{Hs} = 1.8 \times 10^{-3}G$ (where the shear modulus $G = 148$ GPa for MgO). Interestingly, the ratio σ_{Hs}/G agrees well with the value of approximately 5×10^{-3} in stages II and III for fcc metals [53].
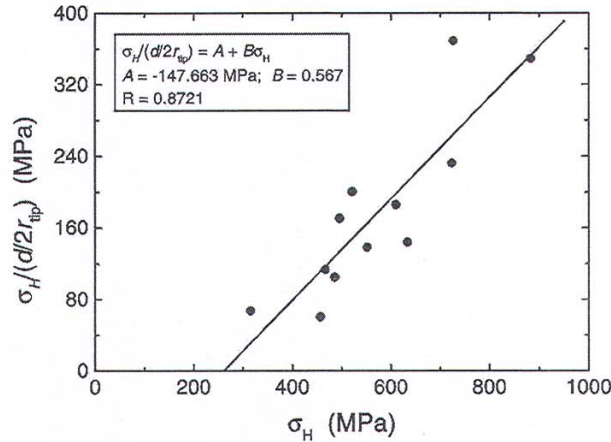

Fig. 18. Plot of the dependence of θ on σ_H as predicted by Eq. (14). After Ref. [23].

The above analysis reveals that the decrease in nanohardness σ_H on the (100) faces of MgO with increasing indentation size a is a result of strain softening process. The observed absence of slip lines around indentation impressions suggests that the softening process involves redistribution of point defects produced during deformation.

3.2. Dependence of hill height on other indentation parameters

From an atomic force microscopy study, Harvey et al. [28] reported that the displacement of material as hills around indents on a surface may be described by Johnson's cavity model and Lockett's model based on the slip-line theory for rigid plastic materials. Fig. 19 illustrates the experimental profiles of the dependence of magnitudes of h on distance r from the centre of an indent on its either sides of trace J and on another trace I while solid lines show the $h(r)$ dependencies predicted by Johnson's and Lockett's models. It may be noted that Johnson's cavity model slightly overestimates the dependence of magnitudes of h on distance r from the indent centre but Lockett's model greatly underestimates the displacements.
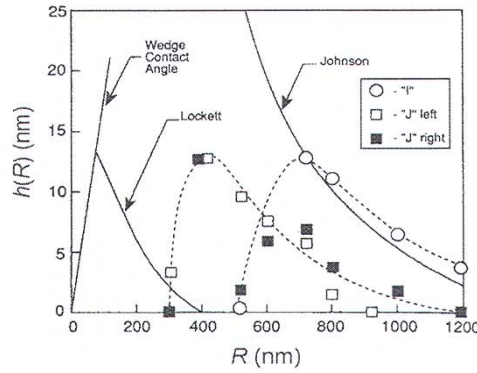
Fig. 19. Experimental profiles of the dependence of magnitudes of h on distance r from the centre of an indent on its either sides of trace J and on another trace I. Solid lines represent the $h(r)$ dependencies predicted by Johnson's and Lockett's models. After Ref. [28].

It was also found that the material of the cavity formed by the indent is piled up around the cavity and that the experimental and theoretical volumes are roughly equal. The equality in experimental and theoretical volumes was suggested to imply that a large fraction of dislocations have emerged at the free surface. In their analysis of the volumes, these authors used Eq. (15), given below.

According to Johnson's cavity model, the relationship between the displacement h of the material piled up as a hill, the indentation diameter a, and the deformation zone radius R is given by [28]

$$\frac{h(a)}{a} = \frac{2\pi(1-\nu)Y}{E^*}\left(\frac{R^3}{a^3} - \frac{1}{8}\right), \tag{15}$$

where indentation diameter $a = 2r$ (r is the indentation radius) and the combined elastic modulus E^* is given by Eq. (4). In principle, this equation is valid only for $R/a \geq 1/2$ (i.e. when $h(a)/a \geq 0$).

Sangwal et al. [23] compared the experimental data on the formation of hills produced around indents on the (100) face of MgO with the predictions of the cavity model. Substitution of the values of $E^* = 115$ GPa, $Y = 80$ MPa [51] and $\nu = 0.3$ in Eq. (15) yields

$$h = 3.06 \times 10^3 a\left(\frac{R^3}{a^3} - \frac{1}{8}\right). \tag{16}$$

Since R/a is practically a constant quantity, hill height $h(a)$ increases linearly with a with a slope $3.06 \times 10^{-3}[(R/a)^3 - 1/8]$.

The slope of the h/a plot from the experimental data is 0.078, which gives the ratio $R/a = 2.95$. This R/a ratio is higher by a factor of 1.8 than the ratio from the experimental data shown in Fig. 16. This difference suggests that Johnson's cavity model relating h and a in the form of Eq. (16) overestimates R (because a can be measured with greater accuracy).

Sangwal et al. [23] proposed a simple physical model, assuming that material of the indentation cavity of volume V_{ind} is forced out from the crystal to form a uniform elevated rim of volume V_{rim} around the cavity. According to this indentation crater model, the hill height may be given by [23]

$$h = \frac{2d}{3\pi\left[(2R/a)^2 - 1\right]}. \tag{17}$$

Since R/a as a constant in the present case, h linearly increases with d. Eq. (17) is valid for $R/a > 1/2$ when $h < \infty$. The linear dependence of h on d may be observed from Fig. 16b.

The slope of h/d plot is $2/3\pi[(2R/a)^2-1)] = 0.071$, which gives $R = a$. Thus, this model reveals that the experimentally measured R values in our case are higher by a factor of 1.67. This means that, in contrast to Johnson's model (Eq. (16)) which overestimates R, Eq. (17) underestimates R. This

discrepancy is probably due to higher values of R and lower values of h in Eq. (17) than the values measured from experiments.

4. Recovery of nanoindentations produced at μN loads

4.1. Surface morphology of recovering nanoindents [30,40,41]

From an in-situ atomic force microscopy (AFM) study of nanoindentations made up to several hundred μN loads on the (111) face of GaAs single crystals, Lilleodden et al. [30] found that with time the indentations recover, leaving the original surface practically in the initial state. These authors explained their observations of the load dependence of indentation size by the Hertzian theory of elastic contacts, and attributed the recovery process to the generation of back stress forces by dislocation half-loops produced by the indenter tip at the indentation bottom.

Recently, Sangwal et al. [40,41] carried out a detailed experimental in-situ AFM study of the morphology and kinetics of recovery of nanoindentation impressions performed on the (100) cleavage faces of MgO crystals for loads up to 10 μN. For the study of recovery kinetics, experimental data on such indentation parameters as indenter penetration depth d, indentation diameter a, deformation zone size R and height h of hills piled up around indents with the time of their recovery were obtained from AFM images recorded immediately after deformation. These parameters are schematically illustrated in Fig. 16a.

It is observed [30,40,41] that the indentation impressions made at low loads are usually circular but they tend to acquire a somewhat asymmetric shape, reflecting the shape of the indenter, at higher loads. The asymmetry becomes pronounced when indentations are made on poorly mounted samples in which a sample drift frequently occurs during indentation and imaging [40]. Typical examples of indents produced on the (100) face of MgO at two different loads of 4.0 and 8.4 μN (Experiments 4 and 7; see Table 1), and their evolution with time are illustrated in Figs. 20 and 21.

Table 1. Values of constants d_0 and n of Eq. (18), h_0 and p of Eq. (21), and the initially applied indentation loads P for different experiments.

Exp	Load P (μN)	d_i (nm)	d_0 (nm)	n	CC*	h_i (nm)	h_0 (nm)	p	CC*
1	1.1	5.8	20.2	0.43	0.9846	0.45	0.84	0.25	1
2	2.1	5.2	13.1	0.45	0.9610	0.27	-	-	-
3	2.8	6.64	61.8	0.83	0.9926	1.05	-	-	-
4 [a]	4.0	17.5	13440	1.31	0.9514	1.54	3.56	0.33	
	0.9695								
5	5.6	28.2	39.2	0.09	0.9076	4.45	9.24	0.18	
	0.9781								
6	6.3	30.7	-	-	-	4.57	14.1 [b]	0.13	
	0.9844								
							112.3 [b]	0.48	
	0.9844								
7	8.4	64.3	-	-	-	13.95	18.94 [c]	0.11	
	0.9617								
						--	237.7 [c]	0.50	
	0.9923								

* Correlation coefficient.
[a] Selected fitting range between $5.6 < \ln t < 8.2$ (t in s).
[b] Fitting ranges below and above $\ln t = 5.8$ (t in s).
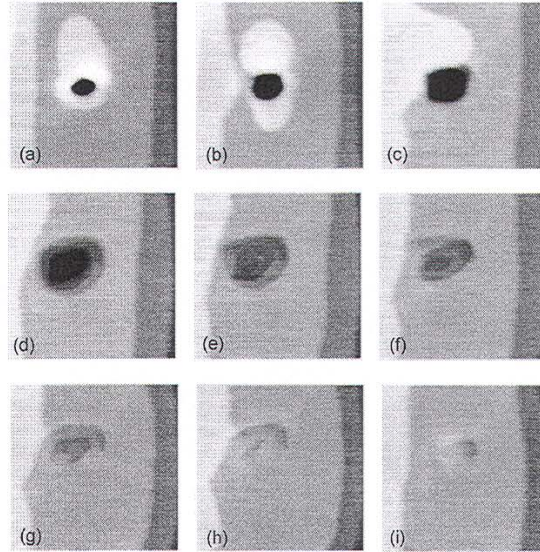[c] Fitting ranges below and above $\ln t = 6.4$ (t in s).

Fig. 20. Evolution of an indentation produced on the (100) face of MgO at a load of 4 μN (Experiment 4) with recovery time: (a) 0 s, (b) 131 s, (c) 360 s, (d) 1211 s, (e) 1669 s, and (f) 2026 s, (g) 2454 s, (h) 2701 s, and (i) 15,835 s. Image size: 600 nm. Note that the indent has a region of protruded material around it as a hill. With reference to vertical elementary cleavage steps of height 0.21 nm it may be seen that no slip traces are produced around the indentation. In the upper parts of (a-c) the large grey areas on the cleavage surface show material "spilt out" from the indentation hill. The height of the layer of this spilt out material is also 0.21 nm. The widening of the diameter of the indentation appears to start from its brim and with time the indentation levels off with the original cleavage surface. After Ref. [40].

In the initial stages every indent has a region of protruded material as a hill around it and the lateral size of this region increases with the applied load (see Figs. 20 and 21). With increasing time, the protruded material first spreads out and subsequently disappears (see Figs. 20 and 21) while the diameter of the indented hole increases. However, the spreading out of the protruded material of the hill occurs at the expense of the hill height (Fig. 21). The sharp "brims" of the indented holes are slowly eroded and the holes widen, while their depth decreases until they disappear practically entirely (see Fig. 20). Examination of sequences of images of recovering indentation holes revealed that initially when a hole begins to widen, the surface close to the brim rearranges into clear unit steps of 0.21 nm height (Fig. 20). The unit steps subsequently separate from the indentation hole in such a manner that the step separation increases with increasing distance from the hole bottom (Fig. 20), and the widening of holes occurs as a result of propagation of steps along the walls of the holes.

During recovery, the shape of the recovering indentations undergoes a change and usually becomes irregular with increasing time (see Fig. 21). Although the size of the indent of Fig. 21 has also increased substantially in the last image relative to the first one, its depth has decreased to 12 nm in the last image recorded after 58,793 s (i.e. after 16 h 19 min 53 s) from an initial depth of 65 nm. This recovery corresponds to an average recovery rate of 1×10^{-12} m/s of the indentation depth. However, slip lines resulting from plastic deformation around the indentations and new elementary steps emerging at the bottoms of recovering indentations are not discerned in the AFM images.
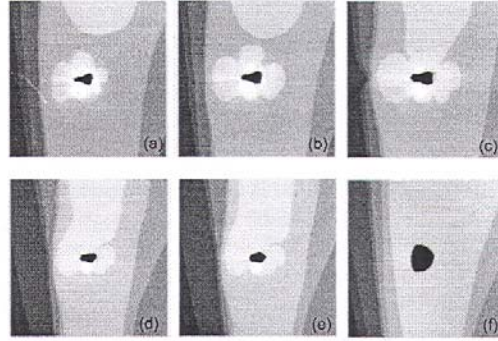
Fig. 21. Evolution of an indentation produced the (100) face of MgO at a load of 8.4 μN (Experiment 7) with time: (a) 473 s, (b) 1583 s, (c) 4048 s, (d) 6175 s, (e) 8648 s, and (f) 58,779 s. Image size: 800 nm. Note that the indentation hill appears even in (e) and the bottom layer of the material of the hillock spreads and joins the rounded step lying in the same level. In (f) both the combined steps have disappeared entirely. With time the elongated triangular indentation shows a tendency to become rounded. On the left side of (c) a well pronounced kink embracing 2-3 steps may be seen. After Ref. [40].

4.2. Kinetics of recovery [40-41]

The basic parameter in indentation experiments is the indentation depth d because all other quantities like indentation diameter a, radius R of deformed zone and hill height h are connected with indentation depth d (see Fig. 16b). In fact, if the initial stage of indentation is taken, the ratio d/D (where D is the indenter tip diameter) may be taken as a measure of effective indentation stress ε (cf. Tabor [1,4]) because the indentation diameter $a = kd$, where k is a dimensionless constant whose value depends on the geometry of the indenter. For example, for the Vickers diamond indenter $k = 7$; while for the indenting tips used in the indentation experiments of MgO, $k = 1.5$ [23]. Since, according to Tabor [1,4]. the effective indentation strain $\varepsilon \approx 0.1a/D$, in the case of MgO indentation experiments $\varepsilon \approx 0.06d/D$.

A typical example of the dependence of d, a, R and h on recovery time t is illustrated in Fig. 22a and b in the form of log-log plots. The figure reveals that d and h decrease with increasing t. However, the decrease is slow up to a time t_1 when the diameter shows a rapid decrease up to another time t_2 beyond which the decrease is again slow. The dependencies of $\ln d$ on $\ln t$ are practically linear in the recovery duration $t_1 < t < t_2$ and $t > t_2$. In contrast to the $d(t)$ plots, a first increases and then decreases, showing a peak at $t = t_2$. Except for the initial stage, the plots of $\ln a$ against $\ln t$ are linear up to about t_2. The dependencies of d on t for $t_1 < t < t_2$ and $t > t_2$ and of a on t in the recovery period $t < t_2$ may be described by

$$d = d_0\, t^n, \qquad\qquad a = a_0\, t^{-m}, \qquad\qquad (18)$$

where d_0, a_0, n and m are constants.

For recovery periods $t < t_1$ the plots of d against t may also be described by Eq. (18), and the value of the exponent in this recovery period is similar to that for $t > t_2$. However, from the data for indentation dwell times $t_{\text{ind}} < 0.1$ s it cannot be discerned because of small values of t_1 [41]. The values of R are roughly of the order of a (see Fig. 22a).
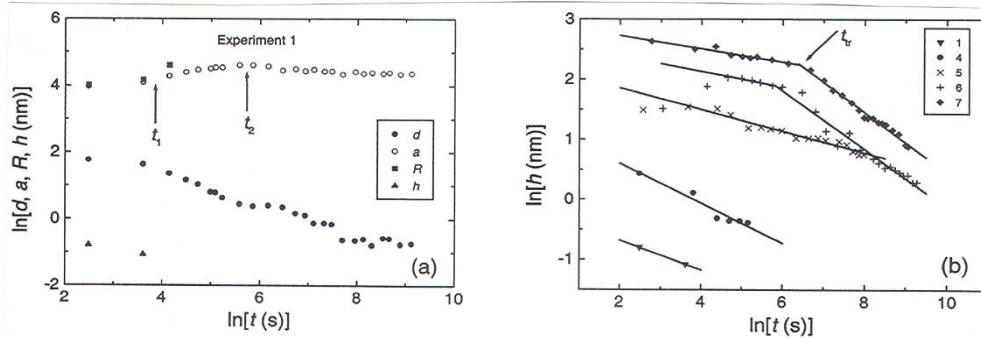
Fig. 22. (a) Dependence of d, a, R and h for indentations on the (100) face of MgO on recovery time t shown as log-log plots for Experiment 1 ($P = 1.1$ μN). (b) Log-log plots of hill height h against t for different experiments. In the $a(t)$ plot of (a) a maximum corresponding to a certain time t_2 (indicated by an arrow) is produced. In (b) an arrow indicates the transition time t_{tr} for Experiment 7. After Ref. [40].

Analysis of the experimental data revealed the following [40,41]:

(1) In the recovery periods $t_1 < t < t_2$ and $t > t_2$, the exponent n has practically constant average values of 0.85 and 0.11, respectively, and the values are independent of the indentation duration t_{ind} and the initial penetration depth d_i. However, the transition times t_1 and t_2 and the extrapolated depths d_0 in both recovery periods increase with increasing d_i i.e. on applied load P and indentation duration t_{ind}.

(2) The average value of the exponent m is 0.22 and does not appear to depend on the initial indentation diameter d_i.

The nature of the $d(t)$ and $a(t)$ plots and the above description of the evolution of indentations with time suggest that during the recovery process a is intimately connected with indentation depth d. Fig. 23a illustrates the dependence of indentation diameters a on indentation depths d for different experiments. The figure clearly shows three regions of d where a difference in the behaviour of the $a(d)$ dependencies may be recognised. In the interval of depth $d < d^*$ (region I), the diameter a of an indentation steeply increases with increasing d up to a depth $d^* \approx 1$ nm when a peak is observed in the $a(d)$ plots. The appearance of well-defined peaks is clearly seen in Fig. 23b. In the second depth interval $d^* < d < d^{**}$ where $d^{**} \approx 17$ nm (region II), the diameter a exhibits a continuous decrease with increasing d. For depth $d > d^{**}$ (region III), the $a(d)$ plots are irregular and no smooth curves are observed (see the data for experiments 5, 6 and 7), although in this case also an increase in a with decreasing d may be noted after extremely long recovery times. For example, after over 16 h the diameter of the indentation of Experiment 7 increased by a factor of 3 but still it was not fully recovered and was about 12 nm deep.

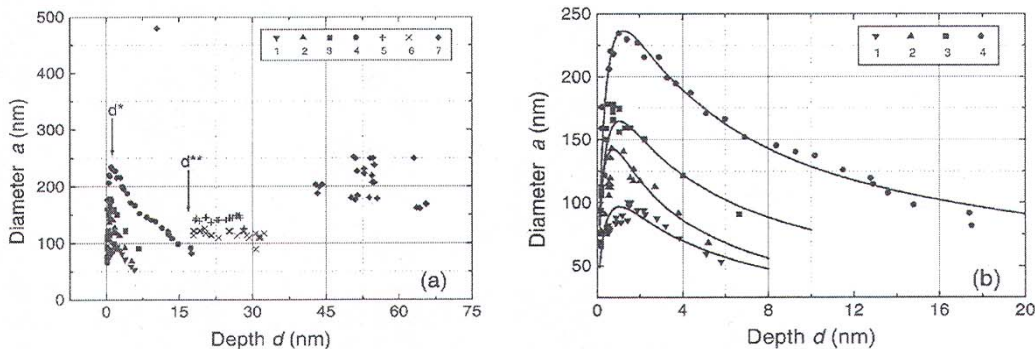Fig. 23. (a) Dependence of indentation diameter a on penetration d for different experiments. Three regions of d may be noted: $0 < d < d^*$ ($d^* \approx 1$ nm), $d^* < d < d^{**}$ ($d^{**} \approx 17$ nm), and $d > d^*$. Penetration depths d^* and d^{**} are indicated by arrows. (b) Dependence of a on d for experiments with initial penetration $d_i < d^{**}$ and data fitting using Eq. (19). After Ref. [40].

In regions I and II, the $a(d)$ data may be described by the relation [40]:

$$a = \frac{a_0 d^{\alpha_1}}{\left(1 + d^{\alpha_1 + \alpha_2}\right)}, \qquad (19)$$

where a_0 is a constant related with the value of a corresponding to $d = d^* \approx 1$ nm while α_1 and α_2 are exponents in the ascending and descending parts of $a(d)$ plots. The curves corresponding to the best-fit values of a_0, α_1 and α_2 are plotted in Fig. 23b.

It was found [40] that the exponents α_1 and α_2 are roughly 0.6 while, as expected, the value of a_0 depends on the initial penetration depth (i.e. applied load P). Combining Eqs. (18) and (19), one obtains an expression relating a with time t in the form:

$$a = \frac{A_1 t^{\beta_2}}{\left(A_2 + t^{\beta_1 + \beta_2}\right)}, \qquad (20)$$

where A_1 and A_2 are new constants while β_1 and β_2 are exponents in the descending and ascending parts of $a(t)$ plots (see Fig. 22a). It was observed that, as in the case of $d(t)$ dependence, the values of A's and β's also increase with increasing value of the initial penetration depth (i.e. with applied load P). Like $\alpha_1 \approx \alpha_2$, $\beta_1 \approx \beta_2$.

By equating the first derivative of Eq. (19) one obtains the transition value of d^* when a peak is formed in $a(d)$ plots, but by equating the first derivative of Eq. (20) one obtains the transition value of t^* when a has a maximum value. The difference in the values of exponent n of Eq. (18) and β_1 and β_2 of Eq. (20) suggest that the recovery of d and a are two different processes following different kinetics, as discussed in Sec. 4.4.

Fig. 22b shows that the hill height h also decreases with increasing recovery time t, and may be described by

$$h = h_0 t^{-p}, \qquad (21)$$

where h_0 and p are constants. The $h(t)$ data for Experiments 6 and 7 reveal that the linear dependencies are followed below and above a transition value of time t_{tr} (indicated by an arrow in Fig. 22b for Experiment 7). For $t < t_{tr}$, the exponent $m \approx 0.12$; but for $t > t_{tr}$, $p \approx 0.5$. The values of p for the data of other experiments lie between 0.12 and 0.5. For large hills the behaviour of the $h(t)$ plots is very similar to that of $d(t)$ plots for large penetration depths. In both cases, the values of the exponents are small up to the transition period but they are relatively high after the transition period (i.e. $n \approx 1$ and $p \approx 0.5$).

From Eqs. (18) and (21) one obtains a relationship between h and d in the form

$$h = h_0 \left(d / d_0\right)^{p/n}. \qquad (22)$$

Since d_0, p and n depend on the initial indentation depth (i.e on applied load), it is difficult to discern a simple relation between h and d. However, it was found that the dependence of h on d for different experiments is practically linear below and above the transition depth d^{**} (Fig. 24). The later stage of the recovery of the hill of Experiment 7 appears to be an exception. The linear dependence of h on d suggests that the exponent of Eq. (22) is approximately unity.

The linear relationship between h and d is consistent with the indentation crater model [23]; see Sec. 3.2. According to this model, the slope of $h(d)$ dependence is $2/3\pi[(2R/a)^2-1)]$. Therefore, when R/a is a constant, h linearly increases with d, as observed in Fig. 24. The slope of the $h(d)$ plot is 0.072 and 0.263 for penetration $d < d^{**}$ and $d > d^{**}$, respectively. The value of the slope for $d < d^{**}$ agrees very well with a value of 0.071 obtained from $h(d)$ plot for the data obtained from unrecovered indentation impressions [23]; see Sec. 3.2.
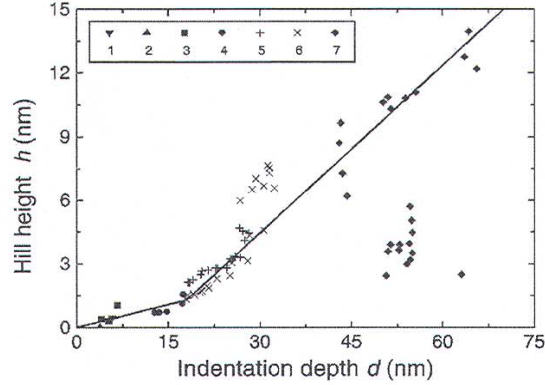
Fig. 24. Dependence of hill height h on indentation depth d for different experiments. Note that the dependence is practically linear with different slopes below and above $d**$. See text for details. After Ref. [40].

From the values of the slope of the plot of h against d one obtains $R = a$ and $R = 2a/3$ for penetration depth $d < d**$ and $d > d**$, respectively. This difference in the behaviour of $h(d)$ plot and in the value of R/a is associated with a difference in the kinetics of recovery of hill height in the two depth regions, as indicated by the exponent p given in Table 1 (see also Sec. 4.4).

4.3. Dependence of indentation pressure on indentation strain [40]

Considering the process of formation of a indentation impression in a crystal surface similar to that of formation of an etch pit at the emergence of a dislocation [54,55], the recovery of indentation impressions with time may be explained. In this model of indentation, the parameters determining the recovery process are: (a) the initial strain ε_i and (b) the pressure barrier $p*$. When $\varepsilon_i > \varepsilon_2$ (i.e. for $d > d**$), stable indentations are formed and recovery is not possible due to the presence of pressure barrier $p*$. However, when $\varepsilon_i < \varepsilon_2$ (i.e. for $d < d**$) recovery of indentations occurs because the process always leads to a decrease in the indentation pressure. Here recovery occurs first as a result of decrease in the indentation surface (contribution p_1) and then due to surface stress (contribution p_0).

Following Tabor [1,4], we define the indentation strain $\varepsilon = kd/D$ and the indentation pressure (stress) $p = \sigma_H = bP/a^2$. Here k is a proportionality constant related with the indenter geometry and D is indenter tip diameter, a is the observed indentation diameter, P is the applied load and b is a dimensionless constant which depends on the indenter geometry. Then it may be considered that the pressure developing under an indentation impression consists of three contributions: (a) surface-layer pressure term p_0, (b) pressure term p_s due to growth of the indentation surface, and (c) pressure term p_v due to growth of the indentation volume. This enables to write indentation pressure as a function of indentation strain ε in the form [40]

$$p = \pi k\lambda d - \pi k^2 \delta d^2 / 4 - C\ln(d/d^*), \tag{23}$$

where λ, δ, C and d^* are constants with units of pressure gradient, impact resistance, pressure and depth. Taking $\varepsilon = kd/D$, this equation may be expressed in the form

$$p = A\varepsilon - B\varepsilon^2 - C\ln(d/d^*), \tag{24}$$

where

$$A = \pi k\lambda D, \qquad B = \pi k^2 \delta D^2 / 4, \tag{25}$$

with units of pressure.

Since a transition in the plot of a against d occurs at $d \approx 1$ nm, in the discussion it may be assumed that $d^* = 1$ nm and $\varepsilon^* = 0.05$. Typical cases of the dependence of indentation pressure p on

indentation strain ε, according to Eq. (23), are illustrated in Fig. 25a. Curve 3 shows the situation when the last term in Eq. (23) is zero, while curves 1 and 2 show the situations when the last term is non-zero. Curves 1 and 2 reproduce approximately the data of Experiments 4 and 3, respectively. Curve 2 differs from curve 1 in a 25% higher A with B and C kept constant.
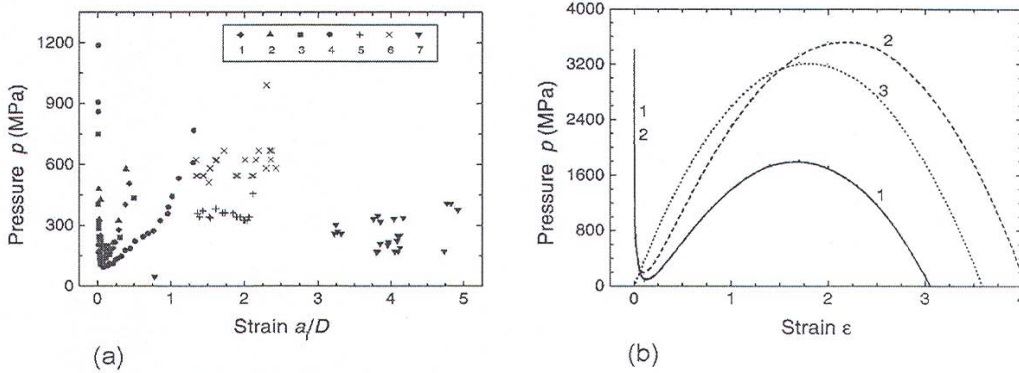

Fig. 25. (a) Plots of indentation pressure p on indentation strain ε for different experiments. Note three regions of the slopes of p(ε) plots: negative for $\varepsilon < 0.06$, positive for $0.06 > \varepsilon > 1.2$, and practically constant for $\varepsilon > 1.2$. (b). Plots of indentation pressure p on indentation strain ε predicted by Eq. (24) for different values of parameters A, B and C: (1) $A = 3600$ MPa, $B = 1000$ MPa and $C = 400$ MPa, (2) $A = 4500$ MPa, $B = 1000$ MPa and $C = 400$ MPa, and (c) $A = 3600$ MPa, B = 1000 MPa and $C = 0$ MPa. Note that the $p(\varepsilon)$ data for different experiments with $0.06 < \varepsilon < 1.2$ can be fitted by changing the values of A, B and C. After Ref. [40].

The behaviour of the dependence of p on ε can be divided into three regions. With increasing ε there is a steep decrease in the value of p in the first region ($\varepsilon < \varepsilon_1$), then it rapidly increases in the second region ($\varepsilon_1 < \varepsilon < \varepsilon_2$) while it decreases in the last region ($\varepsilon > \varepsilon_2$), after passing through a maximum corresponding to ε_{max}. When the logarithm term is negligibly small, the dependence of p on ε up to the strain ε_{max} corresponding to the bulk critical pressure p^*_{bulk} is similar to the well known deformation curves. The critical pressure p^*_{bulk} is the equivalent of the yield point of a crystal. The ideal Hooke's law is valid only at low strains, i.e. in the initial parts of $p(\varepsilon)$ curve when When the linear term is dominant in Eq. (23), the recovery of indentation impressions occurs as a result of decrease in the indentation surface (contribution p_1).

It should be noted that the dependence of p on ε up to the strain ε_{max} corresponding to the bulk critical pressure p^*_{bulk} (curve 3) is similar to the well known deformation curves. The critical pressure p^*_{bulk} is the equivalent of the yield point of a crystal. The ideal Hooke's law is valid only for low strains, i.e. in the initial parts of $p(\varepsilon)$ curve when

The above ideas may be used to explain the process of recovery of indentation impressions. The parameters determining the recovery process are: (a) the initial strain ε_i and (b) the pressure barrier p^*. When the initial strain $\varepsilon_i > \varepsilon_2$, stable indentations are formed and recovery is not possible due to the presence of pressure barrier p^*. In contrast to this, when $\varepsilon_i < \varepsilon_2$, recovery of indentations occurs because the process always leads to a decrease in the indentation pressure. Here recovery occurs first as a result of decrease in the indentation surface (contribution p_1) and then due to surface stress (contribution p_0).

Plots of the experimental dependence of indentation pressure p on indentation strain ε are presented in Fig. 25b. The figure clearly shows that the dependence of p on ε can be divided into three regions. In the first region with $\varepsilon <$ ca 0.06 there is a steep decrease in the value of p with increasing ε. For $0.06 < \varepsilon < 1.2$, p rapidly increases with increasing ε. In the last region for $\varepsilon >$ ca 1.2, p remains practically a constant for a particular initial indentation depth (i.e. a given applied load P).

For initial indentation strain $\varepsilon_i < \varepsilon^*$, the experimental dependence of indentation pressure p on ε for different experiments can be fitted by Eq. (23). The fitting parameters are A, B and C, from

which, using Eq. (25), the indentation stress gradient λ and the impact resistance δ may be calculated. In the case of MgO for curve 1, $\lambda = 3.8 \times 10^{16}$ Pa/m and $\delta = 1.4 \times 10^{24}$ Pa/m^2.

When Hooke's law is valid, it is expected that A is equal to the combined indenter-crystal elastic modulus $E^* = 115$ GPa, given by Eq. (3). Depending on the initial indentation strain, for the experimental data shown in Fig. 23a the value of A lies between 3.6 and 5.5 GPa. This value is lower than that of $E^* = 115$ GPa by a factor of 20 to 30. This discrepancy is associated with the fact that the effective indentation strain is lower by this factor than the experimental values of strain d/D used in the analysis [1,4].

4.4. Diffusion and reorganisation processes during indentation recovery [40-41]

The nature of the plots of d against t (Fig. 22a) is very similar to the characteristic form of a stress relaxation curve while that of the plots of a against t is similar to a typical creep curve [56,57]. The conventional stress relaxation and creep processes involve the participation of glide and climb of dislocations. The observed absence of slip traces around an indentation shows that dislocations do not participate in the series of recovery experiments on MgO crystals. Absence of participation of dislocations in the experiments suggests that point defects play an important role in the recovery of nanoindentation deformation.

From the $d(t)$ and $a(t)$ plots one can clearly distinguish three stages of recovery: (1) an initial transient stage ($t < t_1$), (2) a steady-state stage ($t_1 < t < t_2$), and (3) a slow recovery stage similar to the initial transient stage ($t > t_2$). In all the three stages d decreases with increasing t. However, in the case of $a(t)$ plots, with increasing t the indentation diameter a increases with t in stage (1) but it decreases in stage (3). This suggests that the $a(t)$ kinetics are similar in stages (1) and (3) but the corresponding recovery processes occur in opposite directions.

It was observed [41,41] that in the steady-state region the average exponent n is 0.85 while in the transient and the last slow recovery stages 0.1. In contrast, the average exponent $m = 0.22$. We consider below the possible processes responsible for these recovery kinetics.

The kinetics of a variety of processes occurring at an interface, at boundaries between grains, and in the volume of a system, in general, follow the relation

$$y = kt^{1/x}, \tag{26}$$

where κ is a constant and the exponent x takes values from 1 up to 7 [58]. A linear growth law (i.e. $x = 1$) is followed when the process occurs at the interface, while a parabolic law (i.e. $x = 2$) is observed in the case of volume-diffusion controlled processes. When $x \approx 3$-7 the process is governed by volume and surface diffusion along boundaries between grains. In certain processes like segregation of vacancies to dislocations, the exponent is 2/3. Moreover, in mixed kinetics the exponent x takes intermediate values. From these considerations it may be concluded that with increasing value of the exponent x, the kinetics change in the following sequence: diffusion between grains, volume diffusion and surface diffusion.

During the recovery of indentations on MgO cleavages it is difficult to visualise diffusion between grains in its original sense. However, the process of recovery of large hills produced at loads exceeding 4 μN suggests [40] that recovery takes place by some kind of internal (local) reorganisation of the material (see below). In this case the value of the exponent m is very low i.e. $x \approx 5$-10 [40].

Thus, it may be concluded that the recovery kinetics of penetration depth d are controlled by surface diffusion in stage (2) (i.e. for $t_1 < t < t_2$), and by local reorganisation in stages (1) and (3) (i.e. for $t < t_1$ and $t > t_2$). The recovery kinetics of indentation diameter a follow the same kinetics during $t < t_1$ and $t > t_2$ and are controlled by mixed volume diffusion and local reorganisation.

From Table 1 it may be noted that at low recovery periods both the initial penetration depth d_i and the initial hill height h_i are smaller than the constants d_0 and h_0 of Eqs. (18) and (19). This means that the initial short time is transient and probably involves the reorganisation of the indent and the hill.

The recovery kinetics of penetration depth d are controlled by surface diffusion at low strains (e.g. Experiments 1 and 2), by volume diffusion at intermediate strains (Experiments 3 and 4) and by local reorganisation at high strains (Experiments 5 and 6). In contrast, the recovery kinetics of hill

height h are relatively simple. At relatively low strains, the kinetics are mixed and are controlled by local reorganisation and volume diffusion (Experiments 1 and 4). However, at high strains, they are controlled mainly by local reorganisation for $t < t_{tr}$ while by volume diffusion for $t > t_{tr}$.

The recovery of indentation diameter a follow the same kinetics during the intervals $t_1 < t < t_2$ and $t > t_2$. For example, in Experiment 3 the recovery kinetics are controlled by volume diffusion, in Experiments 1 and 2 by volume diffusion and local reorganisation, while in Experiment 4 by mixed volume and surface diffusion. Thus, here also with increasing strain, in all cases the following sequence is obeyed: local reorganisation, surface diffusion and volume diffusion.

Difference in the slope of the plot of hill height h on penetration depth d below and above d^{**} is associated with processes responsible for the flowing (spreading) out of hills laterally and their subsequent shrinking on the indented surface. A clue to the understanding of these processes follows from the evolution of the surface morphology of hills (Figs. 20 and 21). Immediately after indentation, the tops of the hills have maximum curvatures, which are not minimum energy configurations relative to the underlying cleavage surface. In order to attain a minimum energy configuration, the piled-up amorphous material undergoes local rearrangement and crystallisation. As deduced from large hills, the former process is predominant during the initial stage of recovery ($p = 0.1\text{-}0.2$), while the latter overwhelms the former during the later stage of recovery and is controlled by volume diffusion ($p = 0.5$).

The following observations suggest that all the three processes of local reorganisation, volume diffusion and surface diffusion simultaneously participate during the recovery of nanoindentation deformation:
(a) The surface close to the hole brim rearranges into clear unit steps in the initial stages of recovery (see Figs. 20 and 21).
(b) The step separation increases with increasing distance from the hole bottom (see Fig. 21).
(c) The indentation holes widen as a result of propagation of steps along the walls of the holes. However, the resulting kinetics are controlled by the slowest process.

The values of α_1 and α_2 relating a and d lie between 0.50 and 0.74 and are approximately equal. In fact equal values of α_1 and α_2 of 0.5 are expected because, by definition, indentation pressure $p \propto a^{-2}$ is proportional to indentation strain $\varepsilon \propto d$.

5. Conclusions

In the review the present status of the field of indentation deformation at mN and μN loads is surveyed. Since 1991 when the first papers appeared on depth sensing techniques, the number of papers published in the field has been growing continuously. Among the important findings reported in the field are: (1) the observation of pop-in and pop-out effects (large displacement excursions or major events) and minor events involved at low stresses, (2) nature of the material at the indenter-indentation interface (i.e. phase transformation and twinning caused during indentation), (3) recovery of indentations produced at low loads, (4) similarity of the plots of indentation depth d against recovery time t with stress relaxation curves while that of indentation diameter a against t with typical creep curves, (5) three distinct regions in the plots of indentation diameter a against depth d, and (6) indentation size effect. Most of the above findings can be explained in terms of theoretical concepts based on the generation and multiplication of dislocations. However, the recovery of indentations observed at low loads may be explained by considering back-stress forces produced by dislocations as well as healing of the deformed lattice by diffusion processes.

References

[1] D. Tabor, in Microindentation Techniques in Materials Science and Engineering ASTM STP 889, Eds. P.J. Blau and B.R. Lawn, ASTM, Philadelphia, p. 129, 1985.

[2] A. Gerk, J. Mater. Sci., **12**, 735 (1977).

[3] J. J. Gilman, Austral. J. Phys., **13**, 327 (1969).

[4] D. Tabor, The Hardness of Metals, Clarendon Press, Oxford (1951).

[5] K. L. Johnson, Contact Mechanics, Cambridge University Press, Cambridge (1985).

[6] A. C. Fischer-Cripps, J. Mater. Sci., **32**, 727 (1997).

[7] B. W. Mott, Microindentation Hardness Testing, Butterworths, London (1956).

[8] P. M. Sargent, in Microindentation Techniques in Materials Science and Engineering ASTM STP 889, Eds. P. J. Blau, B. R. Lawn, ASTM, Philadelphia, p. 165, 1985.

[9] W. C. Oliver, R. Hutchings, J. B. Pethica, in Microindentation Techniques in Materials Science and Engineering ASTM STP 889, Eds. P.J. Blau, B.R. Lawn, ASTM, Philadelphia, p. 90, 1985.

[10] J. L. Loubet, J. M. Georges, G. Meille, in Microindentation Techniques in Materials Science and Engineering ASTM STP 889, Eds. P.J. Blau, B.R. Lawn, ASTM, Philadelphia, p. 72, 1985.

[11] S. J. Bull, T. F. Page, E. H. Yoffe, Phil. Mag. Lett., **59**, 281 (1989).

[12] H. Li, A. Ghosh, Y. H. Han, R. C. Bradt, J. Mater. Res., **8**, 1028 (1993).

[13] H. Li, R. C. Bradt, J. Mater. Sci., **28**, 917 (1993).

[14] H. Li, Y. H. Han, R. C. Bradt, J. Mater. Sci., **29**, 5641 (1994).

[15] K. Sangwal, J. Mater. Sci., **24**, 1128 (1989).

[16] K. Sangwal, Mater. Chem. Phys., **63**, 145 (2000).

[17] Q. Ma, D. R. Clarke, J. Mater. Res., **10**, 853 (1995).

[18] Ch. Ullner, L. Hohne, phys. stat. solidi (a), **129**, 167 (1992).

[19] Yu. S. Boyarskaya, Deformirovanie Kristallov pri Ispytaniakh na Mikrotvordost (Deformation of Crystals under Microhardness Testing), Shtiintsa, Kishinev (1972).

[20] E. R. Weppelmann, J. S. Field, M. V. Swain, J. Mater. Res., **8**, 830 (1993).

[21] J. S. Williams, Y. Chen, J. Wong-Leung, A. Karr, M. V. Swain, J. Mater. Res., **14**, 2338 (1999).

[22] S. G. Corcoran, R. J. Colton, E. T. Lilleodden, W. W. Gerberich, Phys. Rev., B **55** (1997) 16056.

[23] K. Sangwal, P. Gorostiza, J. Servat, F. Sanz, J. Mater. Res., **14**, 3973 (1999).

[24] Yu. S. Boyarskaya, D.Z. Grabko, E.I. Purich, J. Mater. Sci., **14**, 737 (1979).

[25] J. Guille, M. Sieskind, J. Mater. Sci., **26**, 899 (1991).

[26] G. M. Pharr, W. C. Oliver, D. S. Harding, J. Mater. Res., **6**, 1129 (1991).

[27] T. F. Page, W. C. Oliver, C. J. McHargue, J. Mater. Res., **7**, 450 (1992).

[28] S. E. Harvey, H. Huang, S. K. Venkataraman, W. W. Gerberich, J. Mater. Res., **8**, 1291 (1993).

[29] W. Zielinski, H. Huang, W. W. Gerberich, J. Mater. Res., **8**, 1300 (1993).

[30] E. T. Lilleodden, W. Bonin, J. Nelson, J. T. Wyrobek, W. W. Gerberich, J. Mater. Res., **10**, 2162 (1995).

[31] P. B. Hirsch, P. Pirouz, S. G. Robert, P. D. Warren, Phil. Mag., A. **52**, 759 (1985).

[32] S. G. Robert, P. D. Warren, P.B. Hirsch, J. Mater. Res., **1**, 162 (1986).

[33] E. Le Bourhis, J. P. Riviere, A. Zozime, J. Mater. Sci., **31**,6571 (1996).

[34] C. Tromas, J. C. Girard, V. Audurier, J. Woirgard, J. Mater. Sci., **34**, 5337 (1999).

[35] C. Tromas, J. C. Girard, J. Woirgard, Phil. Mag. A, in print.

[36] C. Tromas, J. Colin, C. Coupeau, J. C. Girard, J. Woirgard, J. Grilhe, Eur. Phys. Journal: Appl. Phys., in print.

[37] Yu. S. Boyarskaya, R. P. Zhitaru, D. Z. Grabko, V. A. Rahvalov, J. Mater. Sci., **33**, 281 (1998).

[38] B. L. Hammond, R. W. Armstrong, Phil. Mag., **57**, 41 (1988).

[39] S. G. Roberts, Phil. Mag., A **58**, 347 (1988).

[40] K. Sangwal, P. Gorostiza, F. Sanz, Surf. Sci., **442**, 161 (1999).

[41] K. Sangwal, P. Gorostiza, F. Sanz, Surf. Sci., **446**, 314 (2000).

[42] W. W. Gerberich, S. K. Venkataraman, H. Huang, S. E. Harvey, D. L. Kohlstedt, Acta Metall. Mater., **43**, 1569 (1995).

[43] W. W. Gerberich, J. C. Nelson, E. T. Lilleodden, P. Anderson, J. T. Wyrobek, Acta Mater., **44**, 3585 (1996).

[44] J. D. Kiely, J. E. Houston, Phys. Rev., B **57**, 12588 (1998).

[45] J. D. Kiely, R. Q. Hwang, J. E. Houston, Phys. Rev. Lett., **81**, 4424 (1998).

[46] J. D. Kiely, J. E. Jarausch, J. E. Houston, P. E. Russell, J. Mater. Res., **14**, 2219 (1999).

[47] Y. Q. Wu, G. Y. Shi, Y. B. Xu, J. Mater. Res., **14**, 2399 (1999).

[48] J. J. Gilman, J. Mater. Res., **7**, 535 (1992).

[49] A. H. Cottrell, Dislocations and Plastic Flow in Crystals, Clarendon Press, Oxford (1953).

[50] C. A. Brookes, R. P. Burnand, J. E. Morgan, J. Mater. Sci., **10**, 2171 (1975).

[51] P. J. Stablein, J. Appl. Phys., **34**, 1867 (1963).

[52] J. H. Westbrook, Proc. Amer. Soc. Testing Mater., **57**, 873 (1957).

[53] J. Gil Sevillano, in Plastic Deformation and Fracture of Materials, Edited by H. Mughrabi VCH, Weinheim, p. 19, (1993).

[54] N. Cabrera, M. M. Levine, Phil. Mag., **1**, 450 (1956).

[55] K. Sangwal, Etching of Crystals, North-Holland, Amsterdam (1987).

[56] C. Kittel, Introduction to Solid State Physics, 5th edition, Wiley, New York (1976) Chapter 4.

[57] F. R. N. Nabarro, Theory of Crystal Dislocations, Clarendon Press, Oxford (1967).

[58] J. Philibert, Atom Movement: Diffusion and Mass Transport in Solids, Les Editions de Physique, Ulis (1991).